NASA/TM—2012-217269

Investigation of Effects of Material Architecture on the Elastic Response of a Woven Ceramic Matrix Composite

Robert K. Goldberg and Peter J. Bonacuse
Glenn Research Center, Cleveland, Ohio

Subodh K. Mital
The University of Toledo, Toledo, Ohio

January 2012

NASA STI Program . . . in Profile

Since its founding, NASA has been dedicated to the advancement of aeronautics and space science. The NASA Scientific and Technical Information (STI) program plays a key part in helping NASA maintain this important role.

The NASA STI Program operates under the auspices of the Agency Chief Information Officer. It collects, organizes, provides for archiving, and disseminates NASA's STI. The NASA STI program provides access to the NASA Aeronautics and Space Database and its public interface, the NASA Technical Reports Server, thus providing one of the largest collections of aeronautical and space science STI in the world. Results are published in both non-NASA channels and by NASA in the NASA STI Report Series, which includes the following report types:

- TECHNICAL PUBLICATION. Reports of completed research or a major significant phase of research that present the results of NASA programs and include extensive data or theoretical analysis. Includes compilations of significant scientific and technical data and information deemed to be of continuing reference value. NASA counterpart of peer-reviewed formal professional papers but has less stringent limitations on manuscript length and extent of graphic presentations.

- TECHNICAL MEMORANDUM. Scientific and technical findings that are preliminary or of specialized interest, e.g., quick release reports, working papers, and bibliographies that contain minimal annotation. Does not contain extensive analysis.

- CONTRACTOR REPORT. Scientific and technical findings by NASA-sponsored contractors and grantees.

- CONFERENCE PUBLICATION. Collected papers from scientific and technical conferences, symposia, seminars, or other meetings sponsored or cosponsored by NASA.

- SPECIAL PUBLICATION. Scientific, technical, or historical information from NASA programs, projects, and missions, often concerned with subjects having substantial public interest.

- TECHNICAL TRANSLATION. English-language translations of foreign scientific and technical material pertinent to NASA's mission.

Specialized services also include creating custom thesauri, building customized databases, organizing and publishing research results.

For more information about the NASA STI program, see the following:

- Access the NASA STI program home page at *http://www.sti.nasa.gov*

- E-mail your question via the Internet to *help@sti.nasa.gov*

- Fax your question to the NASA STI Help Desk at 443–757–5803

- Telephone the NASA STI Help Desk at 443–757–5802

- Write to:
  NASA Center for AeroSpace Information (CASI)
  7115 Standard Drive
  Hanover, MD 21076–1320

NASA/TM—2012-217269

Investigation of Effects of Material Architecture on the Elastic Response of a Woven Ceramic Matrix Composite

Robert K. Goldberg and Peter J. Bonacuse
Glenn Research Center, Cleveland, Ohio

Subodh K. Mital
The University of Toledo, Toledo, Ohio

National Aeronautics and
Space Administration

Glenn Research Center
Cleveland, Ohio 44135

January 2012

This work was sponsored by the Fundamental Aeronautics Program at the NASA Glenn Research Center.

Level of Review: This material has been technically reviewed by technical management.

Available from

NASA Center for Aerospace Information
7115 Standard Drive
Hanover, MD 21076–1320

National Technical Information Service
5301 Shawnee Road
Alexandria, VA 22312

Available electronically at http://www.sti.nasa.gov

Investigation of Effects of Material Architecture on the Elastic Response of a Woven Ceramic Matrix Composite

Robert K. Goldberg and Peter J. Bonacuse
National Aeronautics and Space Administration
Glenn Research Center
Cleveland, Ohio 44135

Subodh K. Mital
The University of Toledo
Toledo, Ohio 43606

Abstract

To develop methods for quantifying the effects of the microstructural variations of woven ceramic matrix composites on the effective properties and response of the material, a research program has been undertaken which is described in this paper. In order to characterize and quantify the variations in the microstructure of a five harness satin weave, CVI SiC/SiC, composite material, specimens were serially sectioned and polished to capture images that detailed the fiber tows, matrix, and porosity. Open source quantitative image analysis tools were then used to isolate the constituents and collect relevant statistics such as within ply tow spacing. This information was then used to build two dimensional finite element models that approximated the observed section geometry. With the aid of geometrical models generated by the microstructural characterization process, finite element models were generated and analyses were performed to quantify the effects of the microstructure and its variation on the effective stiffness and areas of stress concentration of the material. The results indicated that the geometry and distribution of the porosity appear to have significant effects on the through-thickness modulus. Similarly, stress concentrations on the outer surface of the composite appear to correlate to regions where the transverse tows are separated by a critical amount.

Introduction

Ceramic matrix composites (CMCs) are being investigated for use in high temperature applications. Potential application areas include hot-section engine components such as blades, vanes, combustor liners and nozzles, as well as airframe structural components, particularly for hypersonic applications such as wing leading edges. Ceramic matrix composites offer several advantages over monolithic ceramics including higher stiffness and strength, improved toughness and a more graceful failure mode. However, design and analysis methods for these materials are still under development.

Researchers such as Murthy, et al. (Ref. 1) have found that there is a significant amount of variability in the physical properties of ceramic matrix composites such as elastic modulus and the proportional limit. Morscher, et al. (Ref. 2) (as one example) has determined that the microstructure of a ceramic matrix composite can have a significant effect on the effective properties and response of the material. Furthermore, researchers such as Lamon and co-workers (Refs. 3, 4, and 5) have quantified ways that the damage that takes place on the microscale can be reflected in the effective response of the composite. As shown in Figure 1, a micrograph of a five harness satin weave CVI SiC/SiC composite, the microstructure of a woven ceramic matrix composite displays significant amounts of variability and irregularity in areas such tow spacing, ply alignment, nesting of adjacent plies and matrix thickness. Furthermore, particularly for a CVI SiC/SiC composite, there is a significant amount of porosity that is arranged in irregular patterns. Therefore, a need exists to investigate the effects of the complex material microstructure on the effective properties and life of these materials. In addition, a need also exists to determine how the

characterized variability in the microstructure correlates with the known variability in the material properties of ceramic matrix composites.

As discussed in Nemeth, et al. (Ref. 6) and Mital, et al. (Ref. 7), in many analytical approaches that have been derived to model the response of woven ceramic matrix composites, the representative unit cell (the smallest repeating unit that is assumed to be representative of the composite as a whole) of the composite has been modeled using an idealized, ordered architecture with average dimensions for the tow geometry and spacing. A sample of a finite element model of a five harness satin weave ceramic matrix composite developed using this approach is shown in Figure 2. The regular geometry of the modeled composite can be seen in this figure. The areas between the fiber tows are assumed to be composed of matrix material. The effects of porosity are accounted for by uniformly degrading the properties of the pure matrix regions based on the overall percentage of porosity in the composite.

By comparing the actual microstructure of the composite shown in Figure 1 with the idealized microstructure shown in Figure 2, several key differences can be identified. In the actual composite, the undulation of the woven tows is much more gradual than is seen in the idealized model. In the actual composite, the outer boundary is very uneven due to the methods that are used to infiltrate the matrix material, while in the idealized model the outer boundary is smooth. In the idealized composite, the porosity is assumed to be evenly distributed throughout the composite, while in the actual composite the matrix is located in concentrated areas around the fiber tows, and the porosity is spread throughout the composite in irregular patterns. All of these differences indicate that by idealizing the composite using the methods applied classically, effects of the material response resulting from the irregular material microstructure and its variability on the material response may not be properly captured. The fact that the microstructure of the composite may affect the overall response and damage of the material is hinted at in the analyses discussed in Mital, et al. (Ref. 7), where in the simulation of a tensile test regions of higher stress were found in the areas where the fiber tows crossed over each other.

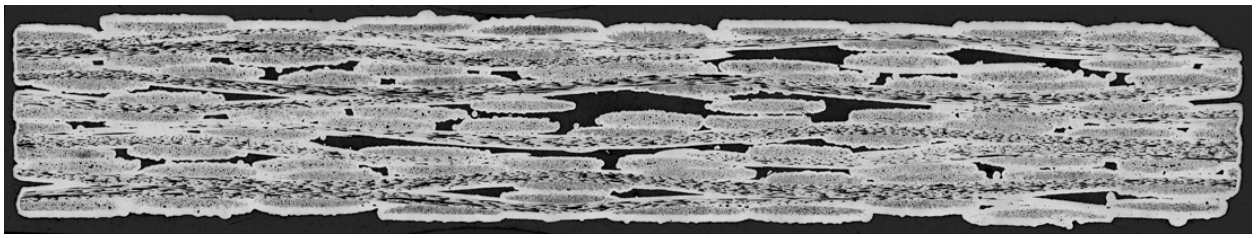

Figure 1.—Micrograph of a five harness satin weave CVI SiC/SiC Composite

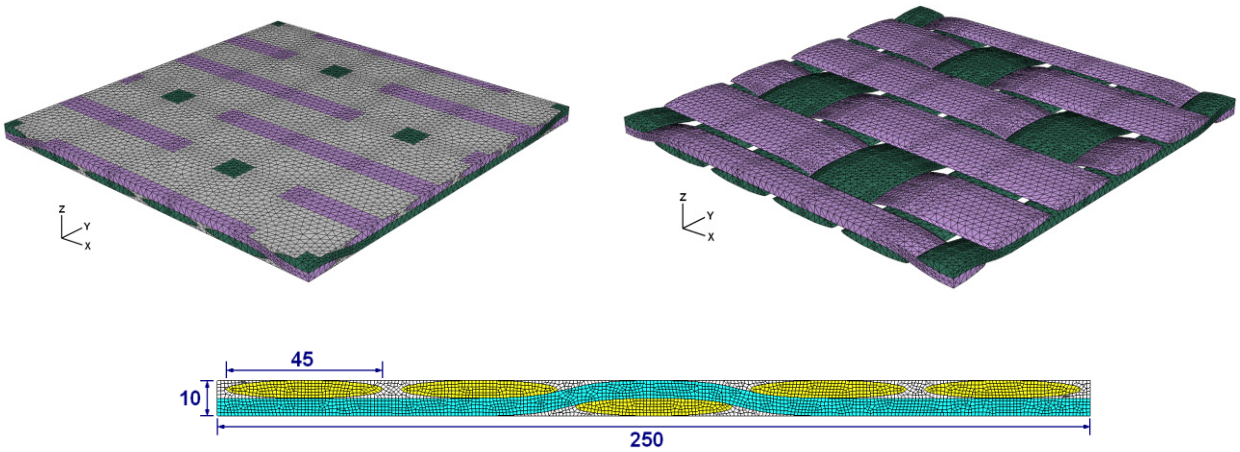

Figure 2.—Finite element models of a woven SiC/SiC composite generated using a classical analysis approach.

To develop a method for quantifying the effects of the microstructure of a woven ceramic matrix composite and its variability on the effective properties and response of the material, a research program has been undertaken which is described in this paper. For this research study, the model material examined is a CVI SiC/SiC eight ply five-harness satin weave material. The composite has continuous Sylmaric-iBN fiber tows (20 ends per inch) woven into a five-harness woven fabric preform in a mutually orthogonal [0°/90°] pattern. A silicon-doped boron nitride (BN) coating was deposited on the surface of the individual filaments within the fiber tows. The fiber preform was infiltrated with a CVI-SiC matrix, which filled the area within the fiber tows and formed a thin coating around the fiber tows. The overall fiber volume fraction was approximately 0.36. Specifically, in this report, methods which have been developed to systematically characterize the microstructure of the material will be described. With the aid of the geometrical models generated by the microstructural characterization process, finite element models were generated and analyses were performed to quantify the effects of the microstructure and its variation on the effective stiffness and areas of stress concentration of the material.

Microstructural Characterization

In order to quantify the ways in which the variation of the microstructure in woven ceramic matrix composites affects the mechanical response of these materials, the variability needs to be accurately quantified. To address this issue, an effort has been undertaken to capture the distributions of various composite architectural parameters such as: distance between tows, size and shape of pores, relative alignment of plies, etc. The first step in this process involved the controlled removal of material from a sample of the composite material, in stages, while collecting high resolution imagery of the subsequently polished surfaces. Quantitative image processing techniques were then used to: correct for uneven illumination, “segment” the pixel intensity groups that correspond to the composite constituent materials, and isolate the “connected” segmented groups (individual pores, tows, etc) in order to systematically identify the constituents of the composite. The details of carrying out this process will be described here. The procedures and algorithms for determining the microstructural parameter distributions in an automated fashion will be the subject of a subsequent report.

Serial Sectioning

For this study, a destructive technique for obtaining high resolution images of the details of the composite microstructure was selected. Samples of the composite were serially polished and high resolution images were acquired at each polishing step. Three specimens of the woven SiC/SiC composite were simultaneously polished, in stages, until the entire specimen was consumed. Figure 3 shows the orientation of the specimen during the polishing procedure, a photograph of the samples in the polishing fixture, and an example of a polished specimen cross section. The target removal rate was 0.2 mm per polished section. Accurate measurements (in three locations around the perimeter) of the height of the sample mounts were taken initially and after each polishing step to determine the amount of material removed. The specimens were initially 12.7 mm square with a thickness of approximately 2 mm. Images of the polished sections were acquired with an optical microscope that had an integrated, motorized, 2 degree-of-freedom translation stage, with associated software, that allowed for the automated acquisition of high resolution images of the whole specimen cross section. Because the camera on this system had a resolution of 640 by 480 pixels (fairly low by current standards) and the features of interest in the composite are relatively small compared to the size of the specimen, a trade-off between the size of the image (amount of memory required to hold the image; the computation time for image analysis tends to increase exponentially with image size) and the needed resolution of the microstructural features had to be determined. After some iteration, an adequate compromise was achieved using a 50 times optical magnification which required 12×3=36 slightly overlapping images to acquire the entire specimen cross section. After stitching the 36 images together, the resulting mosaic came in at about 10 MB (a large image, but still computationally tractable).

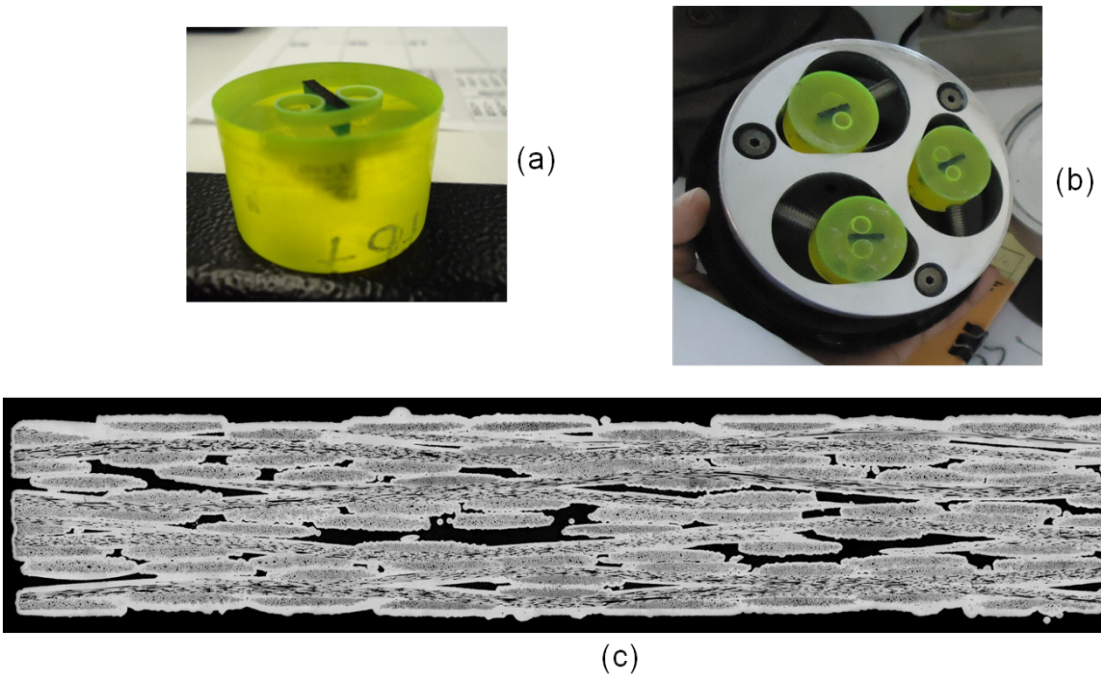

Figure 3.—Specimen mounted in epoxy for polishing (a), three specimens in the polishing apparatus (b), and an example of a polished CVI SiC/SiC composite cross section (c).

Image Segmentation

With the cross section images in hand, the next task was to develop an automated, objective, and repeatable process to identify the composite constituents. This is a necessary step toward the collection of statistics needed for the generation of analysis models for characterizing the effect of microstructural variability. The process of identifying the component parts of an image is often referred to as "segmentation". When there is sufficient separation between the intensities of the various constituents in the image (contrast), it is possible to use statistical techniques to isolate these constituents (Ref. 8). To perform this function, with the goal of having a capability that could be readily shared and expanded by other researchers, it was decided that the implementation should be open source. The Python programming language [http://www.python.org/] was chosen with the addition of the image processing and matrix manipulation tools in the SciPy and NumPy libraries [http://www.scipy.org/]. In the process of implementing the algorithms for the segmentation process, it was found that there was a marked and irregular gradient in the illumination of the specimen. This gradient was first observed when the images making up the specimen cross section were tiled together and there was a noticeable step in the intensity across individual images. To compensate for this, several images of the fairly featureless epoxy surrounding the specimen were acquired to be used for gradient removal. Using a Gaussian blur to smear out the detail in the epoxy images and averaging over the three images gave an approximation of the illumination gradient (Ref. 8). Subtracting the mean of this gradient image from itself gave a matrix of the deviation of the illumination from the mean. This was then subtracted from each of the collected images to correct for the illumination gradient. An image stitching algorithm was also implemented in Python to seamlessly overlay the illumination corrected images into a single image of the specimen cross-section. Figure 4 displays the histogram of the pixel intensities after illumination gradient subtraction. The figure illustrates the identifiable modes in the pixel intensities that are associated with the composite constituents. Using just the intensity information, a simple one dimensional cluster analysis technique was sufficient to separate the modes. The k-means algorithm (Ref. 9) (coded into the SciPy library) does an adequate job of separating the image constituents (pores, boron nitride (BN) fiber coating, and the SiC matrix and fibers (Fig. 5)). Note that specifically identifying and separating out the boron nitride fiber coating is required in order to isolate

the fiber tows. Since the silicon carbide fibers and silicon carbide matrix are essentially the same material, they have similar pixel intensities, making it difficult to identify the fibers separately from the matrix. However, since the boron nitride fiber coating surrounding the fibers has a different pixel intensity, isolating the fiber coating is possible and leads to identifying the fiber tows in the segmented image.

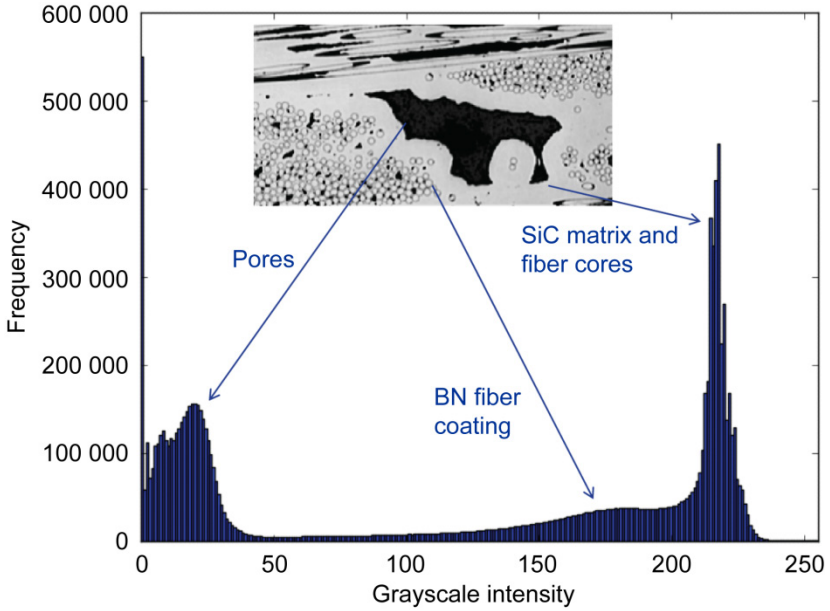

Figure 4.—Histogram of pixel gray scale intensities showing identifiable modes that correspond to the identified composite constituents

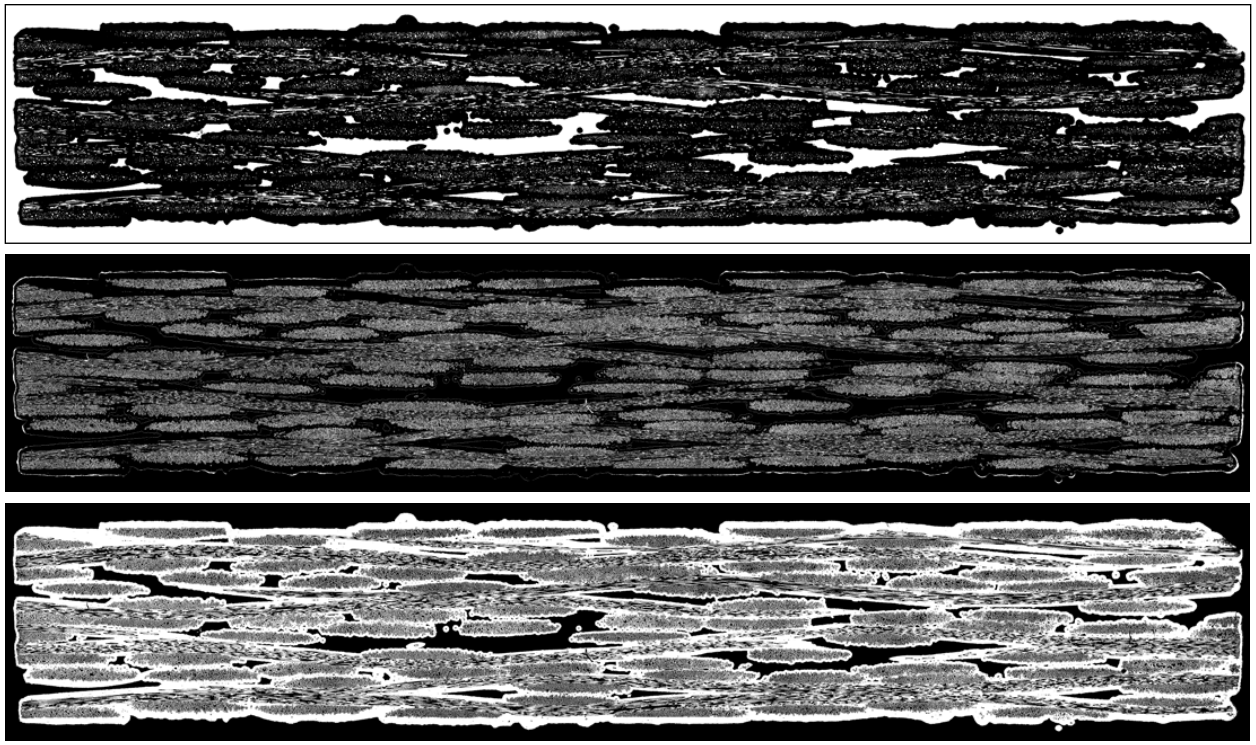

Figure 5.—Three segments of a typical composite cross section isolated using the k-means algorithm: top—porosity; middle—fiber coating; and bottom—SiC matrix and fibers. All three are binary images with the isolated constituent in white.

Quantitative Image Analysis

The next step was to use the information in the segmented images to isolate the microstructural features of interest: transverse sectioned tows, longitudinally sectioned tows, pores, and the SiC matrix surrounding the tows. Using binary morphological operations on selected segments of the images, it was possible to isolate these constituents with reasonable accuracy. The purpose of these morphological operations was to fill in the microstructural features of interest and eliminate the features (at least temporarily) that were not of interest. The transverse tows were isolated first by taking the binary image of just the BN coating segment (all pixels that fell into the fiber coating cluster are "ON" and all other pixels are "OFF"), performing a binary closing (dilation followed by erosion) operation weighted in the horizontal direction to fill in the transverse sectioned tows, followed by a binary opening (erosion followed by dilation) operation weighted to the vertical direction to eliminate the longitudinal sectioned tows. Morphological dilation can be thought of as adding pixels to the periphery of a connected group of pixels. For example, a square group of pixels dilated with a square structuring element would become a larger square grouping. Erosion is simply the inverse of dilation. These operations took advantage of the difference in the shape of these microstructural features. For instance, the fiber coating cluster was chosen for the tow identification because this isolated cluster represented the shapes of the tows best. With a few more filtering operations to eliminate spurious remnants and to fill in and refine the shape resulted in a reasonable approximation of the transverse sectioned tows.

With the transverse tows isolated, an image of the transverse tows was used as a mask for the isolation of the longitudinal tows. Starting again with a binary image of the tow coating segment, the pixels associated with the transverse tows were eliminated with an exclusive OR operation (any pixels ON in both images were turned OFF). Table I contains a brief review of Boolean operations as applied to binary images. Another sequence of binary operations aimed at enhancing and filling in the longitudinally sectioned tows was then performed. To find the matrix, the best solution was to OR the SiC segment with the fiber coating segment (collecting everything that is not a pore) and then to XOR this with the combined isolated transverse and longitudinal tows. This eliminated any overlap that could occur if matrix were to be isolated without any information about the tows. To capture the inter-tow pores in the composite, including those that were surface connected, an operation was performed that set boundaries for the specimen. This was accomplished by again combining the SiC and fiber coating image segments and performing a short sequence of binary morphological operations to fill all the interior voids and close off the surface connected pores. The result of a binary AND operation involving the binary image of the specimen and the inverse of the combined matrix, transverse and longitudinal tows gave an image of the pores. Figure 6 shows the results of the automated constituent isolation for a section.

TABLE I.—BOOLEAN OPERATIONS FOR BINARY IMAGES (PIXELS CAN BE ONLY ON OR OFF)

Operator	Both ON	One ON, One OFF	Both OFF
AND	ON	OFF	OFF
OR	ON	ON	OFF
XOR (exclusive OR)	OFF	ON	OFF

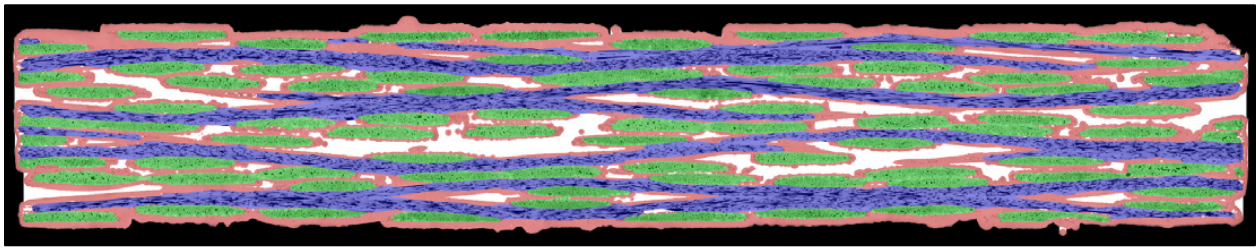

Figure 6.—Composite constituents isolated with an automated procedure utilizing binary morphological operations. Isolated constituents are overlaid on the image of the cross section. Transverse sectioned tows—green; longitudinally sectioned tows—blue; matrix—red; inter-tow porosity—white; and outside specimen—black.

Segmented to Simplified

The images of the isolated composite microstructures were not amenable to the generation of finite element models for structural analysis due to the irregular sizes and shapes of the constituents and, because of ply misalignment, the discontinuous appearance of the longitudinally sectioned tows. To compensate for these irregularities, techniques were developed to generate simplified geometries based on the segmented images while still maintaining relevant microstructural details. This process (illustrated in Fig. 7) started with the transverse sectioned tows. The area and dimensions of the full transverse sectioned tows were determined, taking care to exclude incomplete tows near the cut specimen edges, and used to generate a lenticular shaped object with an area, height, and width equal to mean values of these parameters for the transverse sectioned tows. The centroids of the transverse tows in the segmented image were then determined and copies of the lenticular transverse tow approximation were placed at these centroids as the starting point of the simplified model. The longitudinally sectioned tows were addressed next. Several continuously sectioned tows were found in the sectioned images and a sinusoid was fit to the path of these continuous longitudinal tows. The thickness of the longitudinal sectioned tows was determined by calculating the average thickness of the longitudinal sectioned tows in the segmented images. This thickness value was calculated by summing the number of pixels in each column of the specimen cross section that were identified as belonging to a longitudinally sectioned tow. The mean number of pixels from this calculation was then divided by the number of plies to arrive at an approximate mean longitudinally sectioned tow thickness. Next the specimen micrograph was used to approximate (by eye using open source image editing software, GIMP [http://www.gimp.org/]) the locations of the eight longitudinally sectioned tows. This was complicated by the fact that misalignment of the plies relative to one another caused some longitudinal tows to have only short segments of their paths through the composite exposed in the polished section (see the fourth ply from the bottom in Fig. 7). The transverse sectioned and longitudinally sectioned tow approximations were then overlaid using GIMP and the locations of some of the transverse tows were adjusted to minimize interference with the longitudinal tows and other transverse tows. With this image of the transverse and longitudinal tows as a starting point, the matrix was “grown” uniformly using a function written to dilate the matrix symmetrically on the tows until the matrix volume fraction matched that determined from the segmented image.

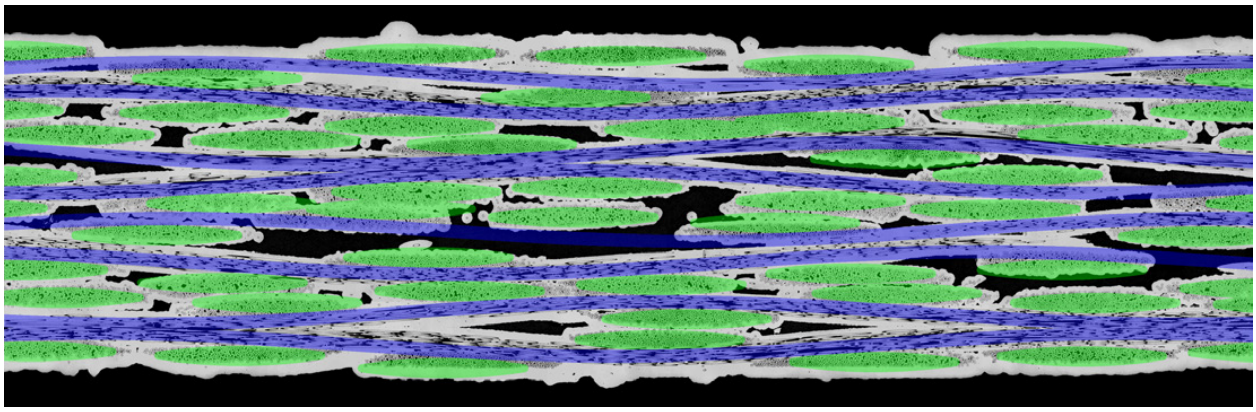

Figure 7.—Transverse and longitudinal tow approximation placement. Note incomplete paths of some longitudinal sectioned tows and displacement of some transverse tows to accommodate continuous longitudinal tows.

Description of Sections and Simplified Idealizations (Volume Fractions, Distribution of Porosity)

Four section images of a single approximately 12.8- by 12.8- by 2.2-mm sample of CVI SiC/SiC composite specimen were selected to generate simplified specimen geometries. Shown in Figures 8 through 11 are the segmented section and the simplified approximation for each of the four sections (designated 03, 10, 22, and 37 based on the sequence of sections taken from the specimen). Four sections were chosen in order to make available for analysis samples with differing microstructures, to facilitate the process of determining how the variation in the material microstructure affects the elastic properties and response of the material. As can be seen in the figures, each of these sections displays a significant amount of porosity arranged in irregular patterns. Furthermore, the fiber tows within a ply display irregular spacing, and the stacked plies are nested within each other. The amount and distribution of the porosity and the relative spacing of the fiber tows can be observed to vary significantly between the various sections. Table II compares the constituent volume fractions calculated from the four actual sample cross sections and the constituent volume fractions in the simplified models (along with analysis results to be discussed later). Note that, unlike classical methods which typically use average values and identical repeating unit cells, the simplified idealizations capture the variations in the composite microstructure observed in the actual specimens. In addition to the four sections generated based on the actual material, an artificially generated "aligned" model was generated using the fit sinusoidal longitudinal tow shape and regularly spaced transverse tows from the simplified specimens, appropriately arranged for a five harness satin weave configuration (Fig. 12). A single unit cell was constructed with these assumptions and used to generate a perfectly aligned and stacked cross section. Note that, as is the case with the composite specimens, alternating plies of the composite are 'flipped', i.e., the satin faces (four tows over in the warp direction) are always mated with adjacent satin faces. This "aligned" model, which still captures key features of the actual microstructure such as the uneven top and bottom surfaces and the large areas of porosity, was created to be used as a baseline to contrast with the more random nature of the idealized, as-manufactured, composite models.

TABLE II.—COMPARISON OF AREA/VOLUME FRACTIONS FOR THE SEGMENTED CROSS SECTIONS AND THE SIMPLIFIED MODELS FROM WHICH THEY WERE DERIVED, ALONG WITH EFFECTIVE MODULUS VALUES

		Pore	Tow	Matrix	Ex, GPa	Ez, GPa
Section 03	Segmented	0.087	0.575	0.338	----	----
	Simplified	0.032	0.630	0.338	237	103
Section 10	Segmented	0.069	0.608	0.323	----	----
	Simplified	0.048	0.628	0.324	227	77
Section 22	Segmented	0.085	0.591	0.324	----	----
	Simplified	0.035	0.639	0.326	234	51
Section 37	Segmented	0.109	0.577	0.318	----	----
	Simplified	0.055	0.623	0.322	229	39
Ideal-01		0.047	0.616	0.338	230	110

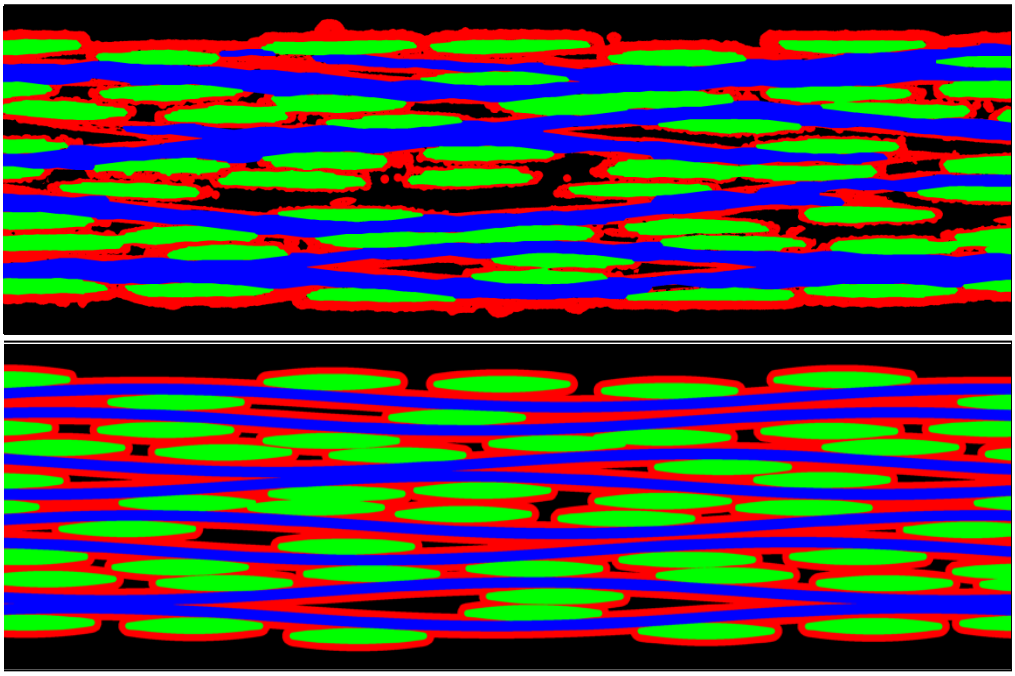

Figure 8.—A comparison between a specimen section and the idealized version constructed for FEM generation (Section 03).

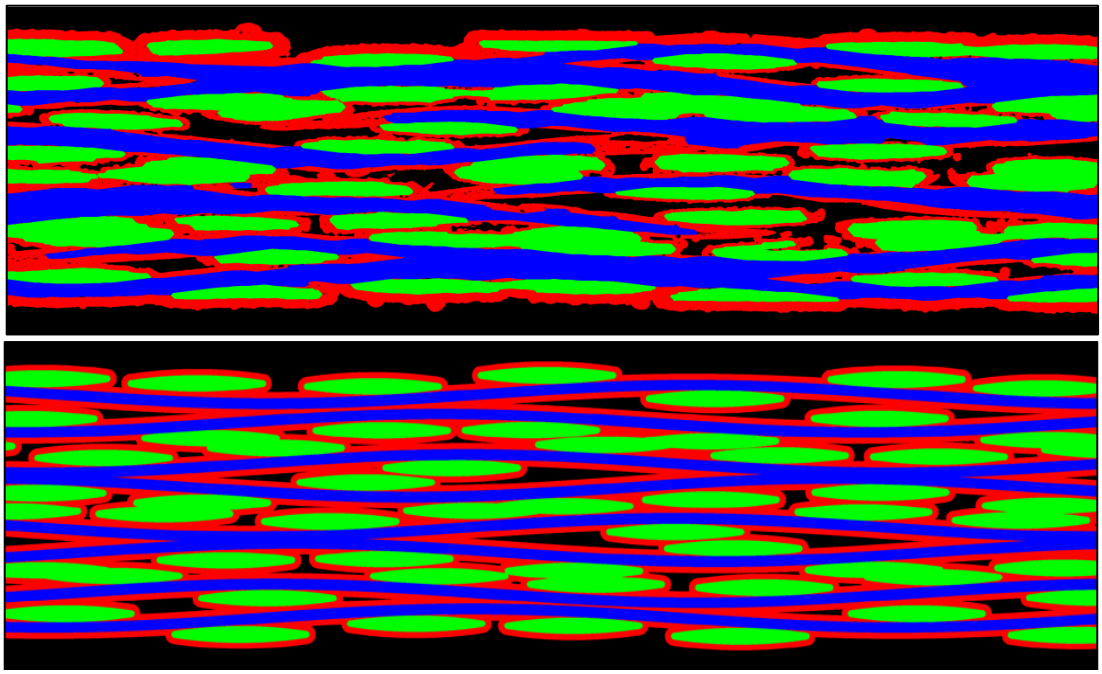

Figure 9.—A comparison between a specimen section and the idealized version constructed for FEM generation (Section 10).

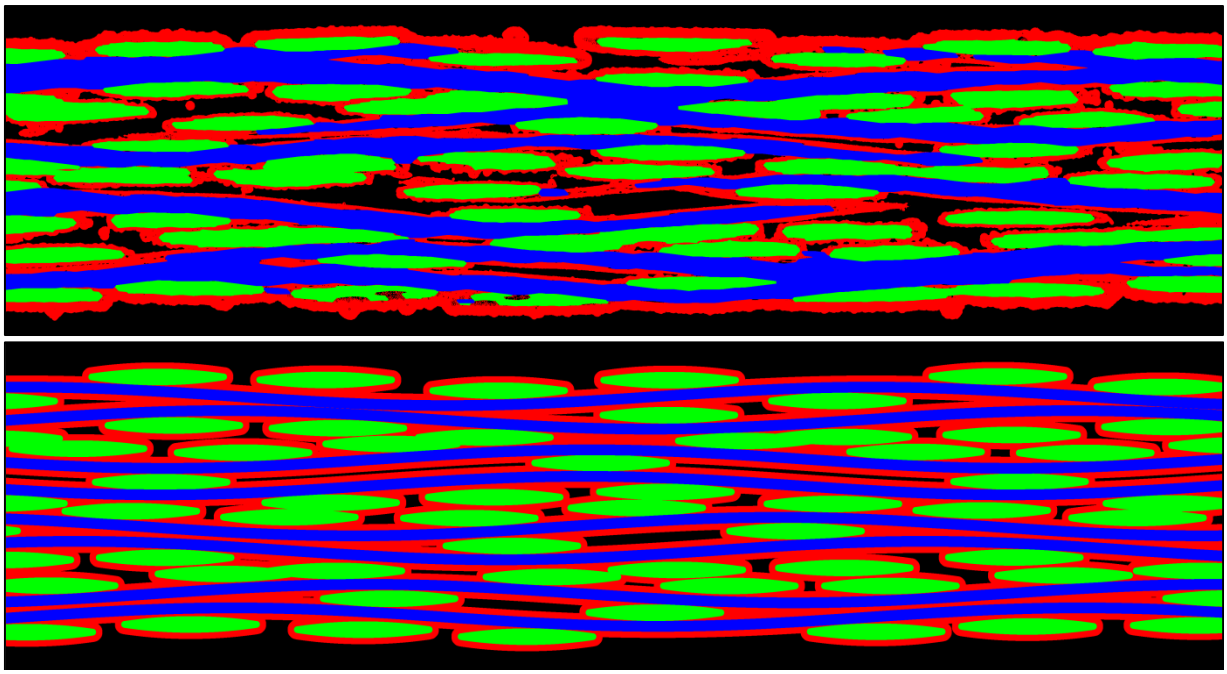

Figure 10.—A comparison between a specimen section and the idealized version constructed for FEM generation (Section 22).

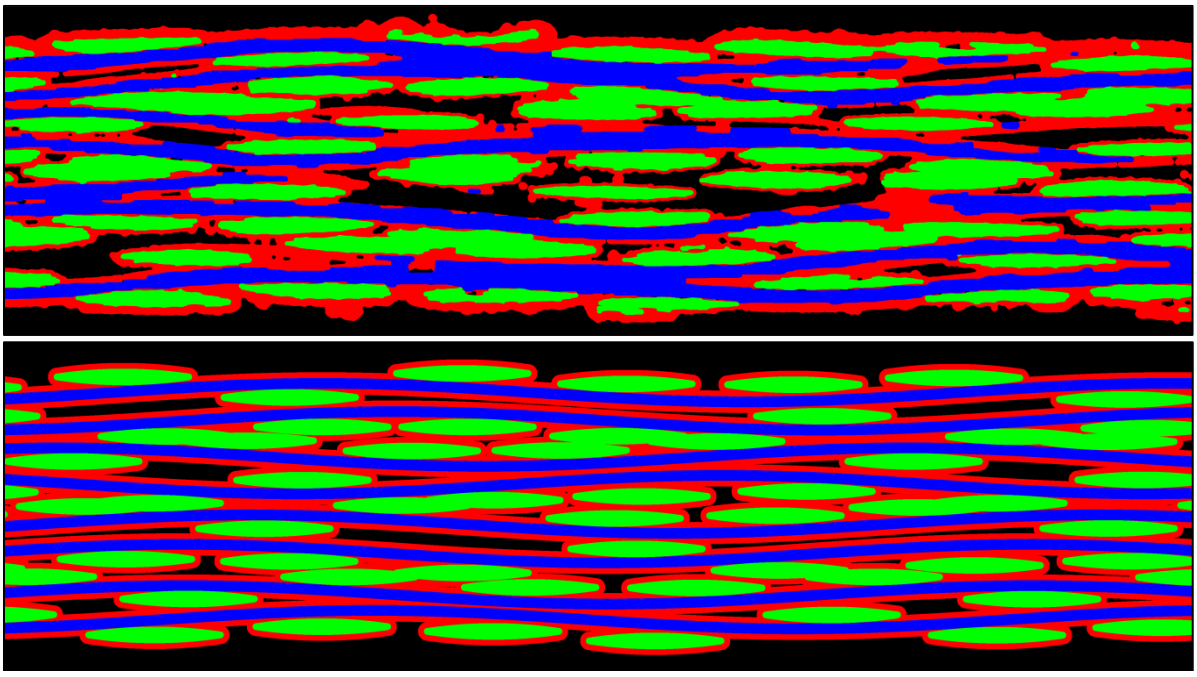

Figure 11.—A comparison between a specimen section and the idealized version constructed for FEM generation (Section 37).

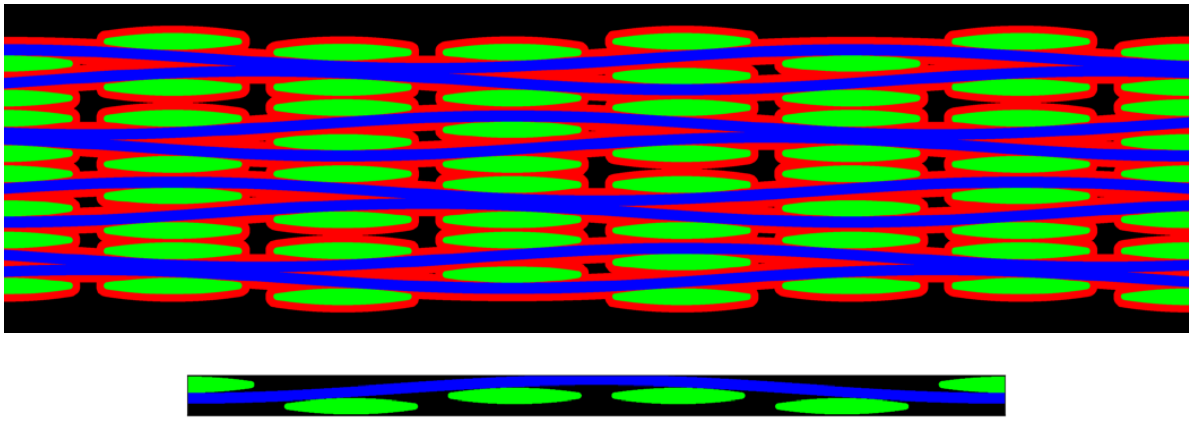

Figure 12.—An aligned CMC approximation constructed from a repeated unit cell that was in turn constructed by placing evenly spaced transverse sectioned tow approximations about the approximation of the sinusoidal fit to the longitudinal tows.

Differences Between Segmented Sections and Simplified Idealizations

In the simplified models, there were several shortcomings of growing the matrix uniformly on the fiber tows. First, the physics of the chemical vapor infiltration process leads to non-uniform deposition of the matrix material on the fiber tows; the matrix is typically thicker on the outer surface of the composite and gets progressively thinner the closer to the centerline. Because of this, the simplified models had a lower porosity than the specimen sections at the same matrix volume fraction. Second, because there was less matrix material on the outer surface of the simplified models, the overall size of the specimen compared to the specimen sections was smaller which, in combination with the lower porosity, led to a high side bias in the tow volume fraction. Also, because the surface tows in the composite tend to be flattened during fabrication, the simplified approximation tended to exaggerate the surface irregularity (especially the deeper intrusions between the tows). When these simplified sections are used as the basis of conducting finite element analyses (which will be described in more detail later in this paper), one consequence of the exaggerated irregularity on the outer surfaces may be that stress concentrations in the matrix near the boundaries of the transverse tows may be somewhat overemphasized.

Another difference between the simplified and actual sections was that that the longitudinally sectioned tows in the simplified approximations did not show the variation in thickness displayed in the sections, both along the length of the tow and from ply to ply. The apparent non-uniform thickness of the longitudinal sectioned tows was mostly due to both the non-uniform cross sectional area of the tows and the slight misalignment of the plies with the sectioning plane causing the apparent thickness of the tow to change. This also contributed to the difference in the porosity between the section images and the simplified models in that the spaces between the longitudinal tows could not be represented in a two dimensional approximation that had continuous longitudinal tows. If the maximum tow thickness were used for the thickness of the longitudinally sectioned tows: 1) it would have presented a packing problem for the simplified model and 2) it would have led to an overestimation of the stiffness in the direction of the longitudinal tows. In constructing the two-dimensional models, few perpendicular sections, through even a perfectly aligned composite, would section the tows through their maximum thickness, therefore an average thickness was necessary to approximate the stiffness appropriately. Future efforts will focus on developing the ability to generate three-dimensional representations of the actual microstructure in order to reduce the effects of these assumptions. Note, however, that even with all of the approximations and simplifications required in the generation of the “simplified” sections, the key features of the material microstructure and their variability were still captured.

Finite Element Analysis

To explore the effects of the complex microstructure of the woven ceramic matrix composite on the effective properties and response of the material, the two-dimensional simplified sections, discussed in the previous section, were analyzed. Two-dimensional finite element models of both the actual and artificially generated "aligned" sections were developed using the software tool OOF2 (Object Oriented Finite Element Analysis of Material Microstructures (Refs. 10 and 11). The finite element models were analyzed using the ABAQUS general purpose finite element program (Ref. 12) in order to examine the effects of the material microstructure and its variability on the effective in-plane and through-thickness moduli, and the location of stress hotspots given a purely elastic load. The stress hotspots would most likely be the locations where damage would initiate in the material under load. For the analyses described in this study, the material response was assumed to be purely elastic. Incorporation of the ability to analyze the progressive damage and nonlinearity in the material response will be described in a future report.

Finite Element Mesh Generation and Model Details

The OOF2 software was used to create the two-dimensional finite element meshes for the two-dimensional sections (slices) examined in this study. OOF2 is a public domain software product created at the National Institute of Standards and Technology (NIST). OOF2 can generate an appropriate finite element model (among other simulation capabilities) starting from a two-dimensional representation, or image, of arbitrary geometrical complexity. For OOF2, the microstructure is a data structure composed of image and property data. The inputs necessary to generate an appropriate mesh include: 1) a microstructure (based on a real micrograph or computer generated image), 2) material properties and 3) boundary conditions. The OOF2 software, which runs on any computer running a variant of the UNIX operating system, is completely scriptable in Python. It can export the finite element meshes generated from the image analysis directly into the ABAQUS finite element program, which can then analyze the meshes generated using OOF2.

The procedure for creating good meshes using OOF2 is quite involved with several steps, and also involves significant user intervention. The process starts by identifying pixels of different colors and assigning them to different groups of materials that will be meshed such as the matrix, longitudinal tows and transverse tows. The process then continues by the generation of an initially very crude mesh, followed by iteratively refining and rationalizing the mesh to remove ill shaped elements with features such as sharp corners or high aspect ratios. The mesh is then homogenized to reduce the elements that are not homogeneous, i.e., contain more than one group of materials. This process then goes on iteratively along with a mesh refinement process to ensure good elements and a high quality mesh. One feature of the software is that the whole process, including user inputs, can be carried out using a user-friendly graphical user interface. All of the user inputs can be recorded in a Python script file akin to a history of commands. If needed this Python script file can then be run in a batch mode to recreate the finite element mesh with no user intervention required. A screenshot of the OOF2 graphical user interface is shown in Figure 13.

Finite element models were generated for the four actual (simplified) sections discussed earlier (and shown in Figure 14(a) to 14(d)) which were designated as Sections 03, 10, 22 and 37. In addition, a finite element model was also generated for the artificially generated "aligned" section identified earlier in this report (and shown in Fig. 14(e)), designated Ideal-01. Analyzing the "aligned" section and comparing the results to those obtained from analyzing the sections based on the actual microstructures facilitated the

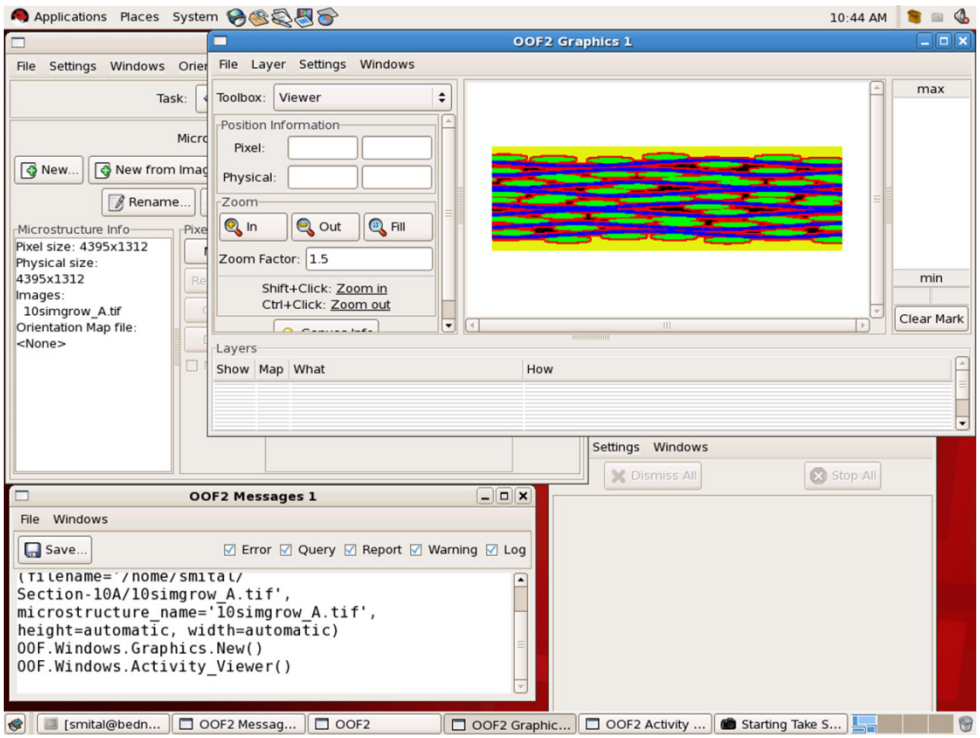

Figure 13.—Screenshot of OOF2 graphical user interface.

process of examining how the variability in the microstructure affected the response of the material. From the simplified images of these sections, image analysis was performed using the OOF2 software and detailed two-dimensional finite element meshes of these sections were created. A typical mesh, a two-dimensional finite element model of Section 03, is shown in Figure 15. The section consisted of longitudinal and transverse tows, CVI-matrix and porosity. To simplify the analysis and keep the size of the finite element mesh reasonable, the longitudinal and transverse tow material was treated as a homogenized material in this model even though the tow consisted of fibers, interfacial coating, matrix and inter-tow porosity. Due to the fact that the areas of inter-tow porosity were found to be relatively small and evenly spaced throughout the fiber tow, the inter-tow porosity was not explicitly modeled, and the effects of the porosity were just accounted for in determining the effective properties of the fiber tows. The finite element model consisted of 17,442 nodes and 19,502 plane stress elements of which 14,545 were linear quadrilateral elements and 4,957 were linear triangular elements. While detailed mesh sensitivity studies were not conducted, the level of mesh refinement used for the analyses were deemed to be adequate. Due to the nature of the simplified models, there were a number of sharp corners near tow boundaries, which could potentially be the source of stress singularities, leading to an inaccurate determination of areas of stress concentrations. However, the level of mesh refinement along and near these corners was assumed to be fine enough to minimize these difficulties. Since the top and bottom surfaces of the sections were not uniform, to allow for applied loads in the through-thickness direction some extra artificial material was added to the sections to make the top and bottom surfaces flat and uniform as shown in Figure 16. When applying in-plane loads in the x-direction (in-plane), this extra material was assigned a very low modulus in the x-direction so as not to change the actual in-plane modulus of the section. On the other hand, when applying a through-thickness load to compute the effective through-thickness modulus, the extra material was assigned a very high z-direction (through-thickness) modulus so that it acted as a rigid material. The modulus of the extra material was kept low in the x-direction. Symmetric boundary conditions were generally used when applying either the in-plane or through-thickness load. For example, when applying in-plane tensile loads in the x-direction, the left edge

was held fixed in the x-direction and the right edge was prescribed a fixed displacement, thus applying a fixed strain on the right edge. Following the finite element analysis, the effective force and thus the stress level corresponding to the applied strain was computed. A similar set of boundary conditions and displacements were applied for computing the through-thickness composite modulus, with the bottom edge being held fixed and fixed displacements being applied on the top edge. As mentioned above, the finite element meshes generated by the OOF2 software were exported to the ABAQUS finite element program to conduct the analyses shown in this work.

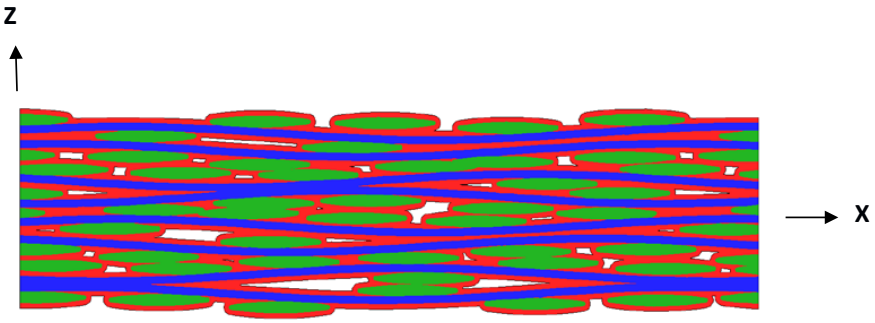

(a) Simplified image of Section 03

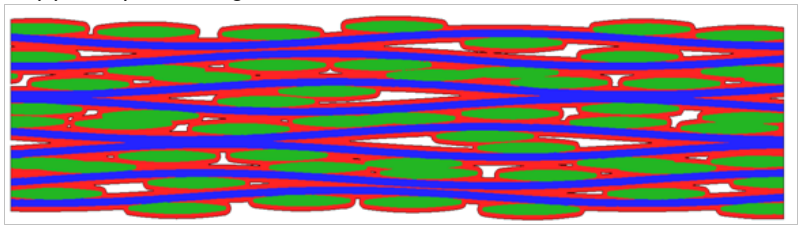

(b) Simplified image of Section 10

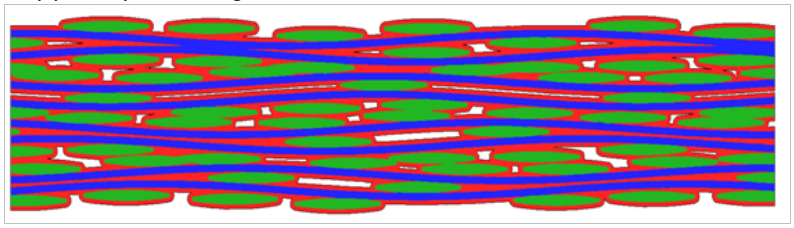

(c) Simplified image of Section 22

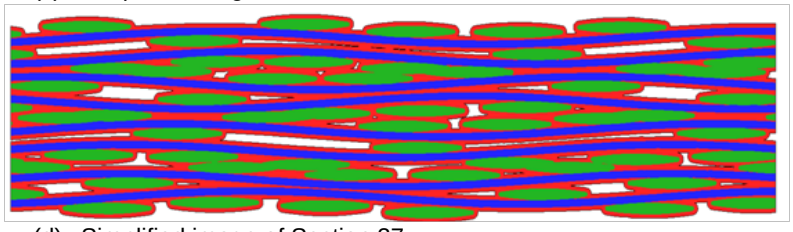

(d) Simplified image of Section 37

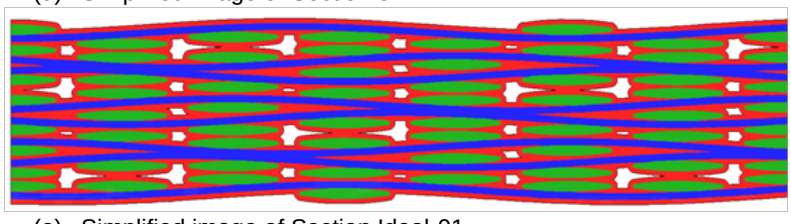

(e) Simplified image of Section Ideal-01

Figure 14.—Images of various sections analyzed (red is CVI-matrix, blue and green are longitudinal and transverse fiber tows respectively, porosity is shown in white space).

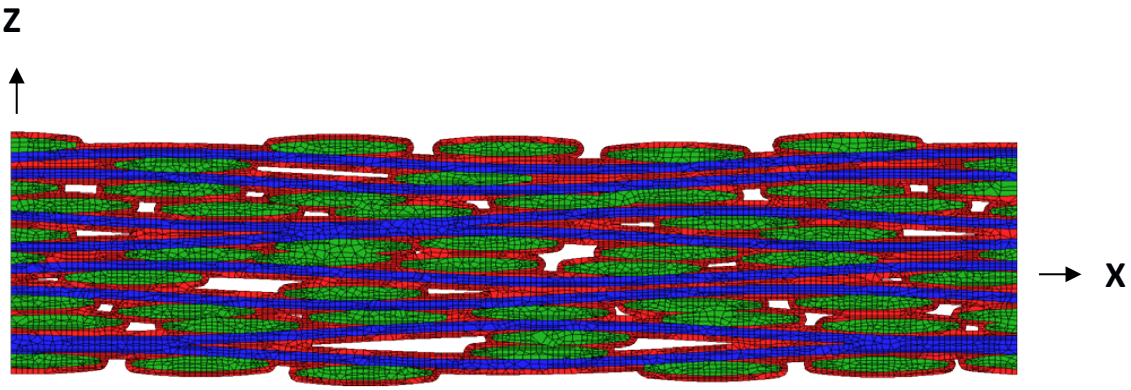

Figure 15.—Finite element model of Section 03 (17,742 nodes, 19,502 elements of which 14,545 are linear quadrilateral and 4,957 elements are linear triangular).

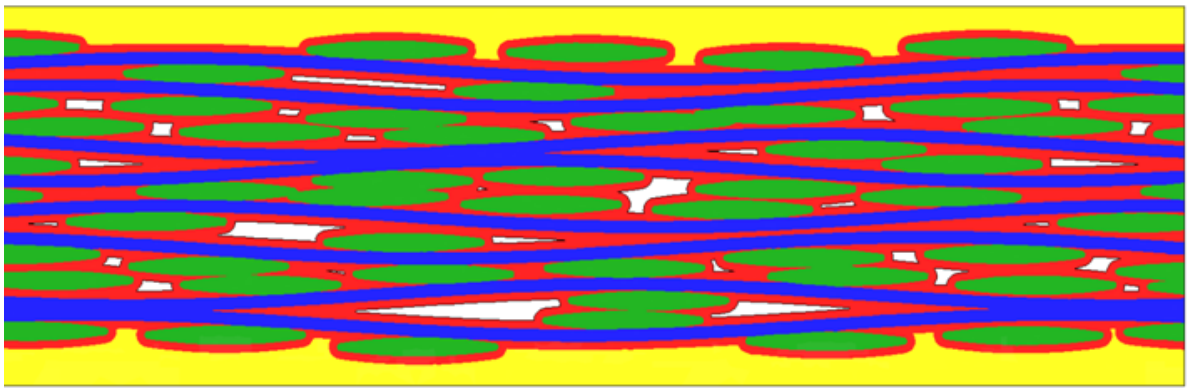

Figure 16.—Simplified image of Section 03 with extra material added (shown in yellow) mainly for through-thickness analysis.

Analysis Results and Discussion

Following the analysis technique outlined above, the in-plane and through-thickness modulus of each of the four actual sections and the "aligned" section discussed above were computed. The constituent material behavior was assumed to be linear elastic. All of the results were computed at room temperature based on room temperature material properties. The effective, smeared properties for the fiber tows were computed based on the fiber, matrix and coating constitutive properties by using classical micromechanics techniques (Ref. 7). The constituent properties of the Sylmaric fiber and boron nitride (BN) coating were assumed to be those given in Mital, et al. (Ref. 7). The fiber tows had a relatively high amount of porosity, on the order of 15 percent, but micrographical examinations revealed that this porosity was relatively uniformly distributed and each pore was relatively small in size compared to the dimensions of the fiber tow. Therefore, in computing the effective tow properties, the elastic properties of the matrix used in the calculations were merely degraded by an appropriate amount to reflect the presence of the porosity. In modeling the matrix material that is present outside of the fiber tows, since the inter-tow porosity is large, unevenly distributed, and explicitly accounted for in the finite element models, the bulk matrix properties were used for this material. The inter-tow porosity was explicitly modeled as holes within the finite element mesh. The effects of the inter-tow porosity were not smeared into the matrix properties as is usually done in classical analysis methods. The computed effective elastic properties of the fiber tows and the bulk matrix properties are given in Table III.

TABLE III.—MATERIAL PROPERTIES USED AT ROOM-TEMPERATURE

Tow Properties 800 filament Sylramic-iBN, Filament diameter = 9.5 μm, BN coating thickness = 0.6 μm, 15 percent porosity (assumed uniformly distributed)	E_L = 260 GPa E_T = 105.5 GPa ν_{LT} = 0.18 G_{LT} = 42.5 GPa
CVI-SiC Matrix	Modulus = 420 GPa Poisson's ratio = 0.2

The effective homogenized in-plane (E_x) and through-thickness (E_z) moduli computed by the finite element analyses for each of the sections are given in Table II. The results indicate that the computed in-plane modulus values displayed a relatively small amount of variability, with the variability that was present being roughly inversely proportional to the amount of porosity in the analyzed sections (i.e., higher levels of porosity yielding lower modulus values). The computed values of the in-plane modulus also correlated with the experimental values (and values obtained by a variety of analytical methods) shown by Mital, et al. (Ref. 7), albeit for a slightly different material. Future efforts will involve obtaining experimental data for the specific material that was examined in this study. The computed through-thickness modulus values, on the other hand, displayed a large amount of variability. Furthermore, the variation in the through-thickness modulus did not directly correlate to the volume fractions of the various constituents. For example, Sections 03 and 22 had very similar amounts of overall porosity but their through-thickness modulus differed by a factor of two. The ratio of the predicted through-thickness modulus to the predicted in-plane modulus obtained in this study was much smaller than the modulus ratio obtained by classical methods for a similar material as shown in Mital, et al. (Ref. 7). Furthermore, the ratio between the mean value of the predicted through-thickness modulus to the in-plane modulus obtained by the current analyses was closer to what was observed experimentally for a similar material described in Mital, et al. (Ref. 7). The maximum through thickness modulus value predicted by the current set of analyses also was much lower than the value predicted using classical methods and much closer to experimentally obtained values.

One possible contributing factor explaining the relatively low predicted values and large variability in the through-thickness modulus computations can be observed by examining contour plots of the transverse displacements for Sections 03 and 22 (which had similar overall amounts of porosity), shown in Figure 17. In Section 22, there were several long, thin areas of porosity, leaving very small continuous areas of fiber tow and matrix from top to bottom in the section, which inhibited load transfer. The lack of load transfer from the top of the section to the bottom resulted in low values of transverse displacement (and by extension low stresses) in the bottom half of the section, with high levels of transverse displacement only in the upper portion of the section, which led to a low through-thickness modulus. In Section 03, on the other hand, the porosity was more uniformly distributed in smaller thicker clumps, leaving more area available for load transfer through the thickness which led to a higher through-thickness modulus, almost double the value obtained for Section 22. However, even in Section 03, the areas of porosity that were present did still serve to inhibit the load transfer to some extent, as reflected in the moderately extended areas of low transverse displacement observed in the contour plot. As mentioned previously, by using traditional analysis methods, much higher relative values of the through-thickness modulus were predicted. The higher relative through-thickness modulus values obtained using classical methods are most likely due to the fact that the porosity is not explicitly modeled in the classical approaches and also that in the classical approaches the fiber tows in each layer are assumed to be perfectly aligned and stacked. Both of these assumptions allow for increased load transfer (and thus overall higher stress levels leading to a higher modulus) to result in the analysis. The effect of fiber tow alignment on the through-thickness modulus can be inferred from the results in the present study where the artificially generated "aligned" Section Ideal-01 had the highest predicted value for the through-thickness modulus. For this section (Ideal-01), since the transverse tows were perfectly aligned

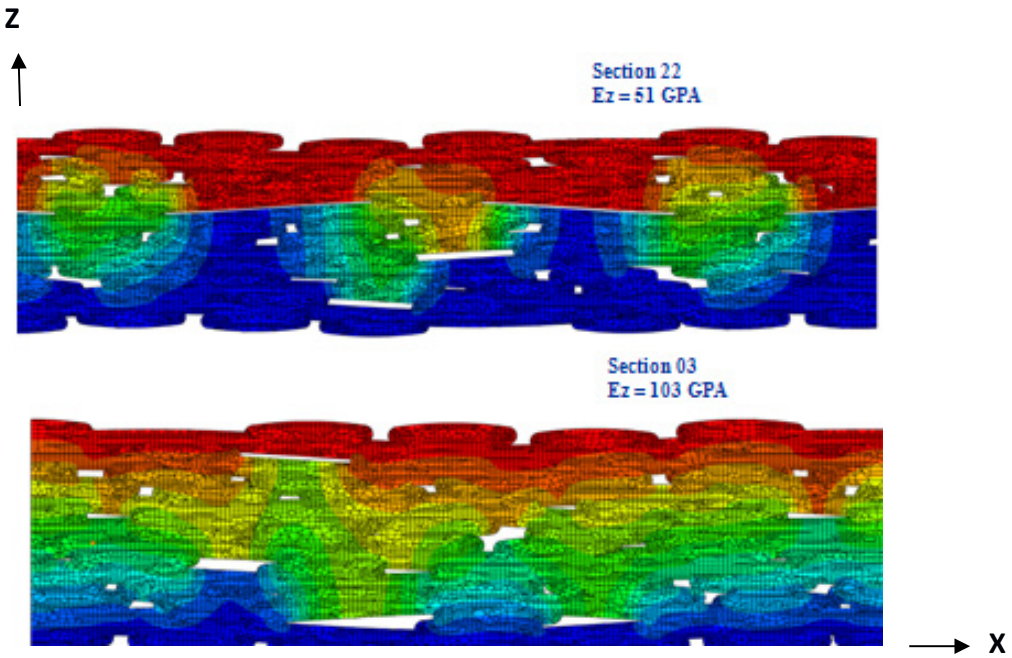

Figure 17.—Through-thickness displacement contours for Sections 03 and 22 (displacement values range from zero (shown in blue) to maximum displacement (shown in red).

and stacked on top of each other, the applied loads could be transferred through the entire thickness, leading to overall higher levels of stress in the entire section and thus higher through-thickness modulus values.

Von Mises and maximum principal stress values resulting from an elastic stress analysis with an applied in-plane strain of 0.07 percent were also plotted for all of the sections analyzed in this study. Due to the fact that only an elastic stress analysis was performed, the level of strain that was applied was somewhat arbitrary. However, this strain value is most likely near the strain level where the stress-strain behavior for the actual composite shows a significant deviation from linear elastic behavior. The purpose of these analyses was to identify the locations of stress risers, to determine if the location of the stress risers were related to any specific architectural feature(s) and to examine the general pattern of stress distribution. The goal of future efforts will be to determine if the predicted locations of the stress risers are the same or related to the locations where cracks are observed to initiate in experimental testing of the actual composite, as cracks would be likely to initiate in high stress locations. Figures 18 through 22 show the von Mises and maximum principal stresses in Sections 03, 10, 22, 37 and Ideal-01 resulting from an applied strain of 0.07 percent in the x-direction. Von Mises stresses were analyzed as a way to quantify an effective stress state resulting from multiaxial loading. While perhaps not completely applicable for the analysis of ceramics and ceramic matrix composites, von Mises stresses could also at least serve as a starting point for the development of damage and failure models. The regions shown in circles are areas of relatively high stresses in these sections. While the specific locations of high stresses vary for each of the sections, for each of the actual sections the areas of high stresses in the matrix on the surface appear to correlate to locations where the transverse tows are separated by some critical distance. There appears to be lower stress concentrations if the transverse tows are farther apart. High stresses in the matrix also were noted in the interior of the sections near some of the areas of large porosity. These points are emphasized in Figure 23, where the maximum principal stresses in the matrix constituent for Section 10 are plotted in a simplified manner, with the high stress regions highlighted in red. As mentioned earlier, these stress concentrations may be somewhat exaggerated due to the exaggerated irregularity in the outer surfaces resulting from the methods used to generate the simplified models. However, the general trends are most likely still valid and correlate with observations that have been made experimentally (Ref. 2). Furthermore, the exact locations of the stress concentrations were located away from the sharp corners

and tow boundaries. Therefore, the stress concentrations were assumed to be real and not the result of stress singularities resulting from the finite element mesh. These preliminary analyses provide indications of how the architecture of the microstructure might affect the initiation of damage in the composite. Further studies are required to rigorously quantify the linkage between architectural features and stress concentrations.

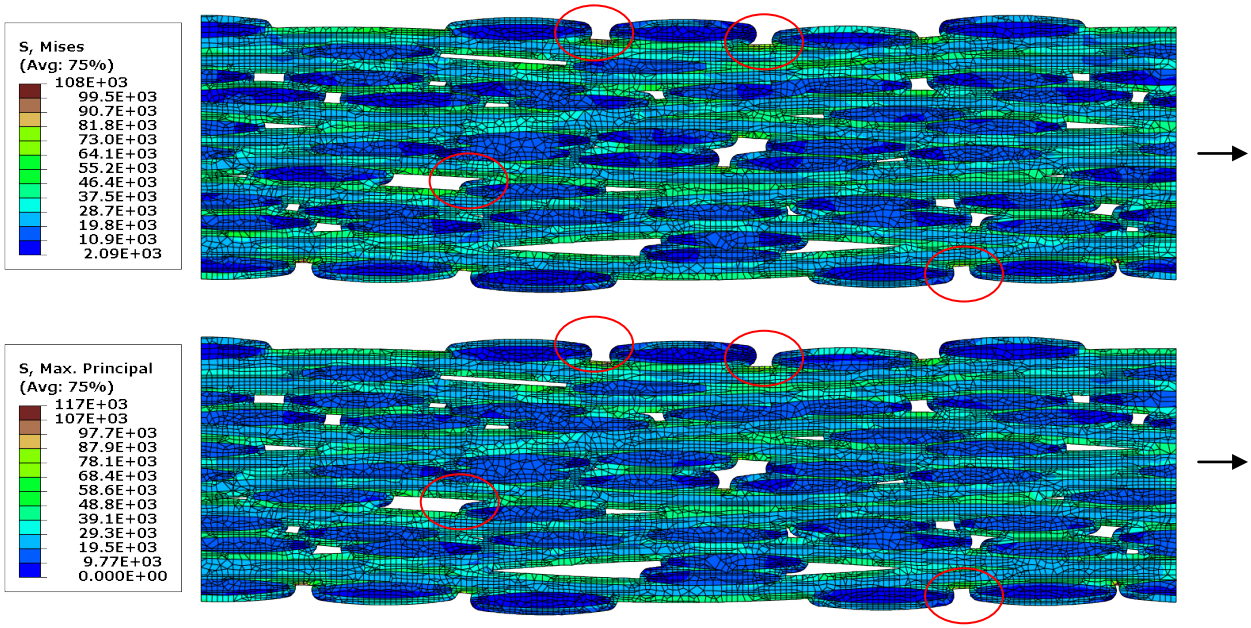

Figure 18.—Von Mises (top) and max. principal (bottom) stresses in Section 03 for applied in-plane strain of 0.07 percent (circles indicate typical locations of damage initiation sites in matrix)

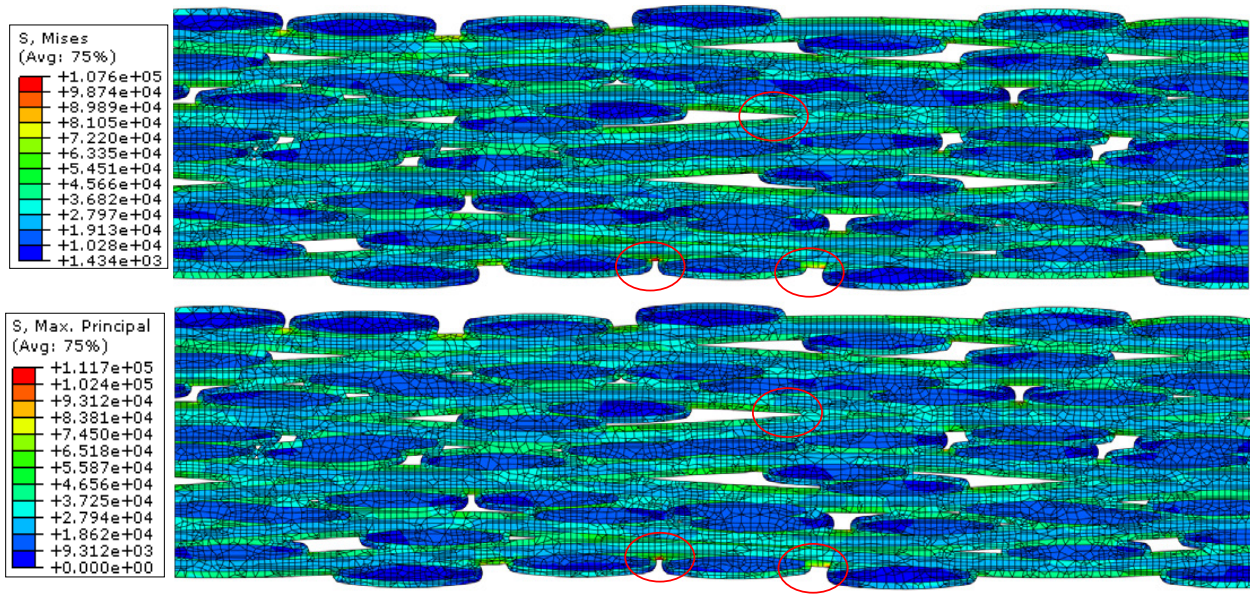

Figure 19.—Von Mises (top) and max. principal (bottom) stresses in Section 10 for applied in-plane strain of 0.07 percent

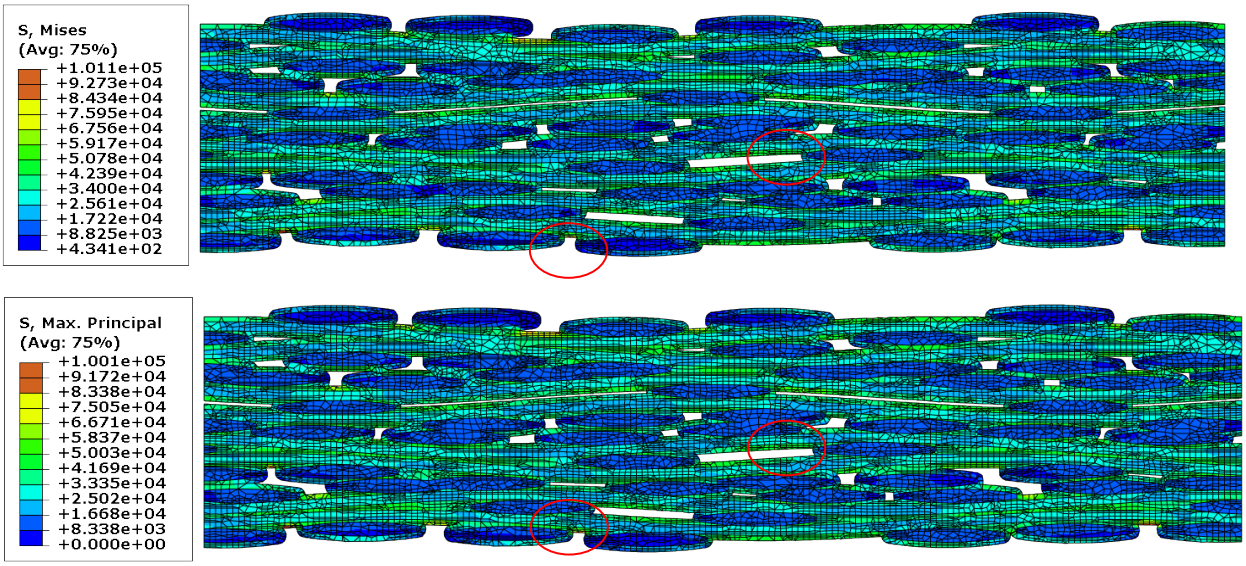

Figure 20.—Von Mises (top) and max. principal (bottom) stresses in Section 22 for applied in-plane strain of 0.07 percent.

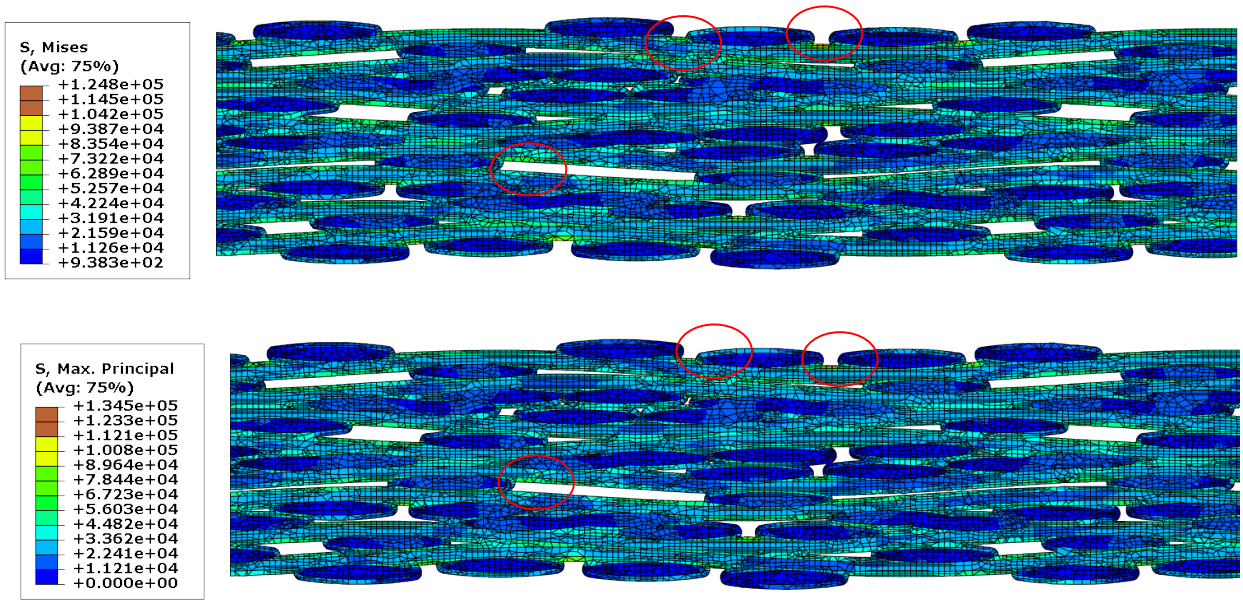

Figure 21.—Von Mises (top) and max. principal (bottom) stresses in Section 37 for applied in-plane strain of 0.07 percent.

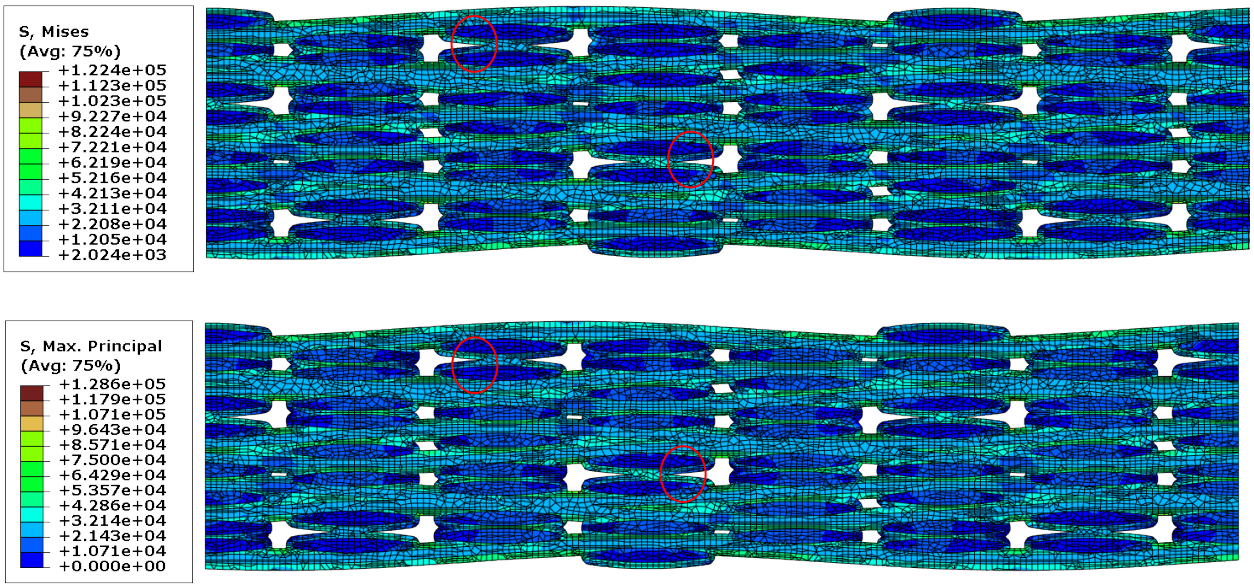

Figure 22.—Von Mises (top) and max. principal (bottom) stresses in Section Ideal-01 for applied in-plane strain of 0.07 percent.

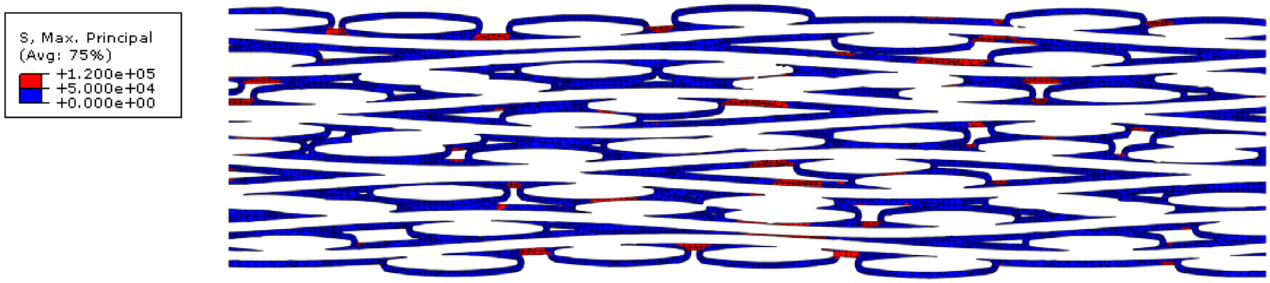

Figure 23.—Plots of high stress regions (shown in red) for the matrix constituent in Section 10.

Cracks in the matrix would most likely initiate from these stress concentration locations, which is why developing a relationship between architectural features and stress concentrations is important. However, an important point to note is that the stress concentration sites in the matrix identified in this study are not necessarily the only potential sites for crack initiation. For example, the stresses in the transverse direction in the fiber tows (related to the x-direction stresses in the transverse tows in the two-dimensional sections discussed here) are also significant. The maximum allowable strain in the transverse direction for the fiber tows is likely to be around 0.05 percent, which when converted to stress is approximately 7.5 ksi. Therefore, even though the actual x-direction stresses in the transverse tows are relatively low in these analyses, the stress levels are actually relatively close to the transverse strength values of the fiber tows indicating that cracks could also initiate in the transverse tows due to matrix cracking or debonding.

Figure 24 shows the distributions of matrix stress in the x-direction due to an applied in-plane strain of 0.08 percent. Matrix stresses were chosen for this plot since these stresses potentially display the greatest variability both within and between sections. Furthermore, since in classical methods the "effective" matrix included both the matrix material and the porosity (in an implicit manner), examining the matrix stresses potentially would illustrate most dramatically the difference between results obtained by modeling the matrix and porosity separately, as is done in this study, and the results obtained using

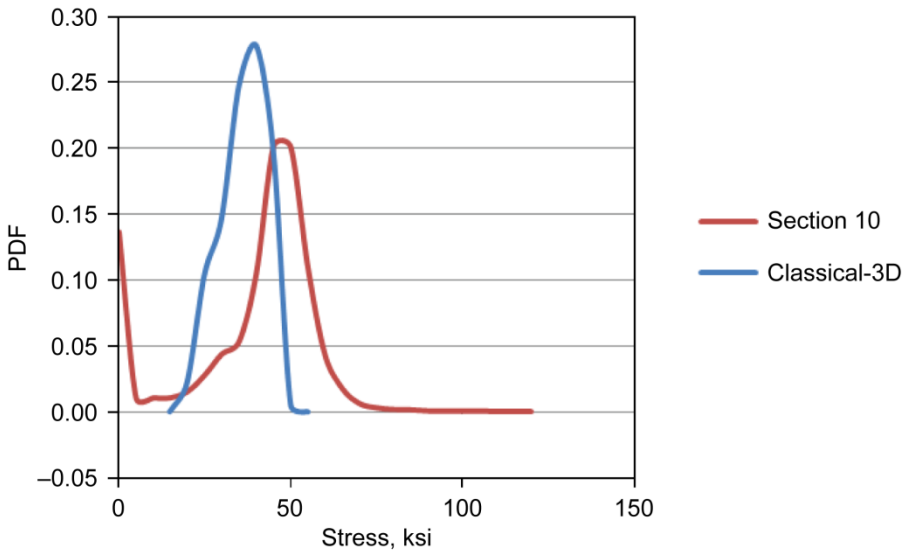

Figure 24.—Probabilistic variation of matrix stress in x-direction (applied strain 0.08 percent) for analyses using actual and classical (idealized) microstructures.

classical methods. The stresses in Figure 24 are plotted both for Section 10 and for an ideal section analyzed using classical three-dimensional finite element analysis. The “classical” analysis model assumed an ordered or nominal architecture and only one ply was modeled. Also in the classical analysis, the porosity was not explicitly modeled but instead was smeared with the inter-tow matrix and degraded matrix properties were used. Even though the results for only one actual section are shown in Figure 24, the results obtained for the other actual sections followed these results very closely. As shown in the figure, the average non-zero stress is higher for the analysis based on the realistic microstructure as compared to the results obtained using classical analysis methods. However, when the second stress peak at zero obtained for the realistic section (resulting from the explicitly modeled porosity) is factored in, the average stress obtained for the realistic section is approximately equivalent to that obtained using classical analysis methods. In the results shown for the classical analysis, since the porosity is incorporated into the effective matrix response, the response of the porosity cannot be explicitly determined. Of more significance, however, is the fact that the results obtained using the realistic microstructure has a distribution with expanded tails and a higher probability of higher stresses as compared to the distribution obtained using classical methods. Since damage would most likely initiate at the areas of high stress, the ability of the analyses conducted utilizing the realistic microstructures to capture the high stress tails of the probability distribution indicates that these analyses would be more likely to accurately identify sites for damage initiation.

Conclusions

A procedure has been developed to systematically characterize the microstructure of a five harness satin weave ceramic matrix composite. In these efforts, representative “slices” of a CMC coupon were examined, both to generate realistic microstructural geometries that could be used for analysis, and to begin to quantify the variability in the microstructure. Using the geometrical models generated by the microstructural characterization process, finite element models were then generated and analyses performed to quantify the effects of the microstructure and its variation on the effective stiffness and areas of stress concentration. By combining the results of the finite element analyses and the microstructural characterization, initial attempts have been made to link the variation in elastic moduli and stress

concentrations obtained by the analyses to specific areas of variability identified by examining the microstructure.

Future efforts will involve more detailed quantification of the microstructural variability both within and between slices. Efforts will also be conducted to modify the procedures used to generate the simplified models to better represent the non-uniform distribution of the matrix throughout the cross-section. Methods to obtain representative three-dimensional images and simplifications of the actual microstructure will also be explored. In the analysis efforts, progressive damage procedures and algorithms will be incorporated into the analysis in order to quantify the effects of the microstructure on initiation and propagation of local damage as well as the first matrix cracking stress and the overall stress-strain response of the composite. Methods to systematically link the variability of the microstructure to the variability observed in the effective properties and response of the composite will also be developed.

References

1. Murthy, P.L.N.; Nemeth, N.N.; Brewer, D.N.; and Mital, S.: "Probabilistic Analysis of a SiC/SiC Ceramic Matrix Composite Turbine Vane," NASA/TM—2004-213331, 2004.
2. Morscher, G.N.; DiCarlo, J.A.; Kiser, J.D.; and Yun, H.M.: "Effects of Fiber Architecture on Matrix Cracking for Melt-Infiltrated SiC/SiC Composites," International Journal of Applied Ceramic Technology, Vol. 7, pp. 276–290, 2010.
3. Guillaumat, L.; and Lamon, J.: "Probabilistic-Statistical Simulation of the Nonlinear Mechanical Behavior of a Woven SiC/SiC Composite," Composites Science and Technology, Vol. 56, pp. 803–808, 1996.
4. Lamon, J.; Thommeret, B; and Percevault, C.: "Probabilistic-statistical Approach to Matrix Damage and Stress-Strain Behavior of 2-D Woven Sic/Sic Ceramic Matrix Composites," Journal of the European Ceramic Society, Vol. 18, pp. 1797–1808, 1998.
5. Lamon, J.: "A micromechanics-based approach to the mechanical behavior of brittle-matrix composites," Composites Science and Technology, Vol. 61, pp. 2259–2272, 2001.
6. Nemeth, N.N.; Mital, S.; and Lang, J.: "Evaluation of Solid Modeling Software for Finite Element Analysis of Woven Ceramic Matrix Composites," NASA/TM—2010-216250, 2010.
7. Mital, S.K.; Bednarcyk, B.A.; Arnold, S.M.; and Lang, J.: "Modeling of Melt-Infiltrated SiC/SiC Composite Properties," NASA/TM—2009-215806, 2009.
8. Russ, J.C.: "The Image Processing Handbook," fifth edition, CRC Press, 2007.
9. Johnson, R.A.; and Wichern, D.W., "Applied Multivariate Statistical Analysis," 5th edition, Prentice Hall, 2002.
10. Langer, S.A. et al.: "OOF: An Image-based Finite-element Analysis of Material Microstructures," Journal of Computing in Science and Engineering, Vol. 3, Issue 3, pp. 15–23, 2001.
11. Reid, A. et al.: "Modeling Microstructures with OOF2," Int. J. Materials and Product Technology, Vol. 35, pp. 361–373, 2009.
12. ABAQUS General Purpose Finite Element Program. Version 6.8, SIMULIA, Providence, RI, 2009.

REPORT DOCUMENTATION PAGE	Form Approved OMB No. 0704-0188

1. REPORT DATE *(DD-MM-YYYY)*	2. REPORT TYPE	3. DATES COVERED *(From - To)*
01-01-2012	Technical Memorandum	

4. TITLE AND SUBTITLE
Investigation of Effects of Material Architecture on the Elastic Response of a Woven Ceramic Matrix Composite

5a. CONTRACT NUMBER

5b. GRANT NUMBER

5c. PROGRAM ELEMENT NUMBER

6. AUTHOR(S)
Goldberg, Robert, K.; Bonacuse, Peter, J.; Mital, Subodh, K.

5d. PROJECT NUMBER

5e. TASK NUMBER

5f. WORK UNIT NUMBER
WBS 599489.02.07.03.02.11.01

7. PERFORMING ORGANIZATION NAME(S) AND ADDRESS(ES)
National Aeronautics and Space Administration
John H. Glenn Research Center at Lewis Field
Cleveland, Ohio 44135-3191

8. PERFORMING ORGANIZATION REPORT NUMBER
E-18025

9. SPONSORING/MONITORING AGENCY NAME(S) AND ADDRESS(ES)
National Aeronautics and Space Administration
Washington, DC 20546-0001

10. SPONSORING/MONITOR'S ACRONYM(S)
NASA

11. SPONSORING/MONITORING REPORT NUMBER
NASA/TM-2012-217269

12. DISTRIBUTION/AVAILABILITY STATEMENT
Unclassified-Unlimited
Subject Categories: 24 and 39
Available electronically at http://www.sti.nasa.gov
This publication is available from the NASA Center for AeroSpace Information, 443-757-5802

13. SUPPLEMENTARY NOTES

14. ABSTRACT
To develop methods for quantifying the effects of the microstructural variations of woven ceramic matrix composites on the effective properties and response of the material, a research program has been undertaken which is described in this paper. In order to characterize and quantify the variations in the microstructure of a five harness satin weave, CVI SiC/SiC, composite material, specimens were serially sectioned and polished to capture images that detailed the fiber tows, matrix, and porosity. Open source quantitative image analysis tools were then used to isolate the constituents and collect relevant statistics such as within ply tow spacing. This information was then used to build two dimensional finite element models that approximated the observed section geometry. With the aid of geometrical models generated by the microstructural characterization process, finite element models were generated and analyses were performed to quantify the effects of the microstructure and its variation on the effective stiffness and areas of stress concentration of the material. The results indicated that the geometry and distribution of the porosity appear to have significant effects on the through-thickness modulus. Similarly, stress concentrations on the outer surface of the composite appear to correlate to regions where the transverse tows are separated by a critical amount.

15. SUBJECT TERMS
Ceramic matrix composites; Woven composites; Finite element analysis

16. SECURITY CLASSIFICATION OF:			17. LIMITATION OF ABSTRACT	18. NUMBER OF PAGES	19a. NAME OF RESPONSIBLE PERSON
a. REPORT	b. ABSTRACT	c. THIS PAGE			STI Help Desk (email:help@sti.nasa.gov)
U	U	U	UU	30	19b. TELEPHONE NUMBER *(include area code)* 443-757-5802